A promising sputtering route for dense Cu$_2$ZnSnS$_4$ absorber films and their photovoltaic performance

Bao-Tang Jheng [a], Po-Tsun Liu [b],[*], Meng-Chyi Wu [a]

[a] *Department of Electrical Engineering, National Tsing Hua University, Hsinchu City, Taiwan*
[b] *Department of Photonics & Display Institute, National Chiao Tung University, Hsinchu City, Taiwan*

A B S T R A C T

Copper zinc tin sulfide (Cu$_2$ZnSnS$_4$, CZTS) is highly abundant in nature. It is an important absorber material for the development of low-cost and sustainable next-generation I$_2$–II–IV–VI$_4$ thin-film solar cells because it has a the tunable direct band gap energy, inexpensive constituent elements, and a large absorption coefficient in the visible wavelength region. This work develops an efficient one-step vacuum-based approach to depositing CZTS films without the need to supply excess sulfur during/after deposition or to perform any post-sulfurization treatment. This one-step RF sputtering process produces CZTS films that are crystalline, phase-pure, dense, smooth, and continuous. Air Mass 1.5 G power conversion efficiencies of as high as 6% have been achieved with an antireflection coating, demonstrating that this new approach has great potential as a low-cost alternative for high-efficiency CZTS solar cell production.

© 2014 Elsevier B.V. All rights reserved.

1. Introduction

Copper ternary chalcogenide compounds and alloys are among the most promising absorber materials for use in photovoltaic (PV) devices, because their energy band gaps can be directly tuned by adding additional elements such as group III elements; they have high optical absorption coefficients in the visible to near infrared spectral range, and they have moderate surface recombination velocities and radiation hardness. The best chalcopyrite CuInSe$_2$ (CISe)-type thin film solar cells with Ga-containing absorber layers of CuInGaSe$_2$ have already demonstrated a conversion efficiency of up to 20.3% [1] and excellent longevity. However, challenges include environmental issues and the scarcity, expense and rarity of the constituent elements. The constituent elements of chalcopyrite-type compound CuInGaSe$_2$ are expensive (In and Ga) and toxic (Se), inhibiting cost-effective large scale production. Therefore, a high-quality semiconductor that comprises abundant elements with low toxicity is a favored alternative for large-scale commercial applications.

The alternative kesterite-type compound Cu$_2$ZnSnS$_4$ (CZTS) is a quaternary semiconductor that is derived from CIS by replacing In (III) with Zn (II) and Sn (IV) in the ratio 50:50. It contains elements that are abundant in the earth's crust and has an ideal direct band gap in the range 1.0–1.5 eV and a large absorption coefficient ($\sim 10^4$ cm^{-1}) [2,3]. Besides, the widely accepted Shockley–Queisser limit conversion efficiency of CZTS solar cells reaches 28% [4]. All of these advantages make it one of the most promising materials for thin film solar cells. Many deposition methods have been used to grow CZTS films, including sputtering, evaporation, electrodeposited, sol–gel, liquid-processing, pulsed laser deposition, etc. [5–15]. The record efficiency of 11.1% for CZTS thin film solar cells was achieved by Todorov et al. through non-vacuum methods [16], and the highest efficiency of CZTS thin film solar cells fabricated through vacuum based methods reaches 9.3% so far [17]. Currently, the production of Cu$_2$ZnSnS$_4$ thin-film solar cell devices as described in the literature cited above faces some problems. These include (i) the high price of precursor material, the toxicity of the required organic solvents, and the quick agglomeration of particles at high temperature; (ii) the need for high-temperature sulfurization, which involves the addition of toxic (N$_2$+H$_2$S) gas and sulfur vapor, in the subsequent stage of deposition of precursor layer; and (iii) the formation of the precursor by the stacking of layers, such as of Cu, CuS, ZnS and ZnSn, which make the process complex and the composition stoichiometry difficult to control. The ultimate aim of this study was the development of a relatively simple and stable growth technique for the production of device quality CZTS thin films. Unlike the methods that were developed in the works cited above, the approach herein is a single-stage sputtering process that involves no sulfurization; has a low production cost, and does not use a solvent that pollutes the environment. Therefore it is highly suited the commercial mass production of solar with a large area.

* Corresponding author. Tel: 886-3-5712121 ext. 52994.
 E-mail address: ptliu@mail.nctu.edu.tw (P.-T. Liu).

In this work, a next-generation CZTS solar device is fabricated using a state-of-the-art technique, which combines quaternary and binary alloy material by co-sputtering. Kesterite phase CZTS absorbers are formed even without additional sulfur supply during/after deposition or a post-sulfurization process. Under proper processing conditions, deposition results in highly-oriented, dense, polycrystalline CZTS films that, when used in photovoltaic devices, yield efficiencies as high as 6% with ZnO nanorod arrays antireflection coating.

2. Experiments

The CZTS solar cell devices in this study have been deposited on 1-mm-thick soda–lime glass substrates cleaned by ultrasonic agitation in a water/detergent solution, followed by rinsing in high-purity water. A bi-layered Mo electrode of 0.8-μm-thick was deposited by a DC magnetron sputtering system. The CZTS films were grown at 500 °C on Mo-coated SLG substrates with the area of 5×5 cm^2 by using RF magnetron sputtering in pure Ar gas atmosphere. All CZTS films were deposited under the following deposition conditions: RF power of 80 W was applied to the quaternary CZTS alloy target, while 15 W, 25 W, and 35 W RF power was used for the binary ZnS alloy target. Substrate temperature was maintained at 500 °C during the sputtering process. An additional etching step was performed in a KCN-containing aqueous solution (10% KCN) to remove segregated $Cu_{2-x}S$ on the surface. The 60-nm-thick CdS layer was grown by chemical bath deposition (CBD). The bath was maintained at 70 °C and contained deionized H_2O, NH_4OH (31.25 mL, ACS reagent from Aldrich), 0.015 M $CdSO_4$ (99% ACS reagent from Aldrich) solution, and 1.5 M thiourea (99% from Aldrich) in deionized water. A 50 nm thick intrinsic-ZnO and a 250 nm thick conductive-ZnO:Al (Al_2O_3 2 wt%) film were deposited in sequence by using RF magnetron sputtering at room temperature as window layers. The growth of ZnO nanorod was to prepare a subwavelength structure on the top of the CZTS devices, and AZO window layer served as a seed layer for the hydrothermal growth of ZnO nanorod (AZO/nanorod). CZTS solar devices were immersed in the aqueous solution of zinc nitrate hexahydrate $(Zn(NO_3)_2 \cdot 6H_2O)$ and hexamethylenetetramine $(C_6H_{12}N_4$, HMT) mixture of the concentration of 0.01 and 0.01 M, respectively. A pH value of 8.5 produced the best results in terms of ZnO nanorod morphology by using 1,3-diaminopropane (DAP, Acros). After completing the nanorod growth, all devices were cleaned with deionized water to remove residual salt. For J–V measurement, individual cells with a total active area of 0.4 cm^2 were defined by mechanical scribing. To efficiently collect photocurrent of CZTS devices, Al front contact grid structures were evaporated on the top of conductive AZO layer before the growth of ZnO nanorod.

The surface morphology was investigated with a Field-emission scanning electron microscope (FESEM) (JEOL JSM-7401F) from Japan Company, using a 10 kV acceleration voltage. Compositional profiles were acquired by FESEM/EDX (energy dispersive X-ray spectroscopy). Localized compositional analysis by energy dispersive X-ray spectroscopy (EDS) was performed in a JEOL JSM-7401F FE-SEM fitted with an Oxford INCA Energy X-ray analyzer at selected positions across the samples. X-ray diffraction (XRD) patterns were obtained with an automated Bruker D8 advance using Cu Kα radiation at 40 kV and 30 mA. Raman spectra were measured using a micro-Raman spectrometer (Jobin Yvon T64000) using an Ar ion laser ($\lambda = 514.5$ nm) as an excitation source. The chemical binding energy of the films was identified by X-ray photoelectron spectroscopy (XPS, ULVAC-PHI, PHI Quantera SXM). Optical transmittance and reflectance were measured at normal incidence in the wavelength range 300–800 nm with a Cary 500 UV–visible–near infrared spectrophotometer equipped with an integrated sphere. The current density–voltage (J–V) curves of photovoltaic devices were obtained by a Keithley 4200 source-measure unit. The photocurrent was measured under simulated 100 mW cm^{-2} air mass 1.5 global (AM 1.5 G) irradiation using a xenon lamp-based solar simulator at 25 °C using a temperature controller.
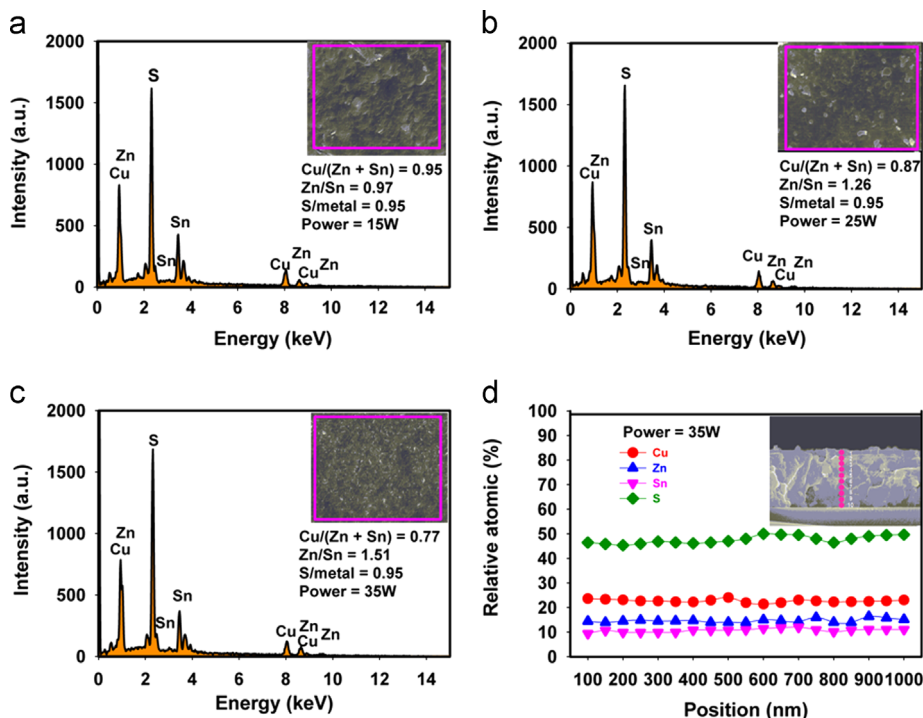

Fig. 1. Energy-dispersive spectrometer (EDS) composition analysis of annealed CZTS films deposited at various co-sputtering powers: (a) 15 W, (b) 25 W, and (c) 35 W. (d) Elemental profiles determined by EDS scan.

3. Results and discussion

Fig. 1a–c presents the composition variation of Cu_2ZnSnS_4 thin films prepared at different co-sputtering powers. The computed stoichiometry shows a variation in both the Zn/Sn and Cu/(Zn+Sn) ratios. The evaluation of the metal ratios [Cu]/([Zn]+[Sn]) and [Zn]/[Sn] in CZTS layers is a critical point since improved performance in solar cells has been attributed to a Cu-poor and Zn-rich absorber layer. Top-view EDS measurements at 15 kV and 10 μA for surface imaging, give [Zn]/[Sn]=0.97 and [Cu]/([Zn]+[Sn])= 0.95 for Fig. 1(a), [Zn]/[Sn]=1.26 and [Cu]/([Zn]+[Sn])=0.87 for Fig. 1(b), [Zn]/[Sn]=1.51 and [Cu]/([Zn]+[Sn])=0.77 for Fig. 1(c). Constituent elemental sulfur element was observed in all Cu_2ZnSnS_4 films without additional sulfurization. The results herein reveal that the Cu/(Zn+Sn) ratio of sputtered films was in the range 0.77–0.95 using a simple co-sputtering process. As the co-sputtering power increased to 35 W, the Cu/(Zn+Sn) ratio dropped significantly to 0.77 (Fig. 1c), owing to a substantial change in the concentrations of both Cu and Zn elements. Meanwhile, the Zn/Sn ratio changed greatly from 0.97 to 1.51 because the concentration of the Zn element changed greatly as the co-sputtering power increased. In the work, a Cu:(Zn+Sn):S atomic ratio of approximately 1:1:2 was observed for co-sputtering power of 25 W (Fig. 1b). A calculation from first principles reveals that Cu-poor and Zn-rich conditions improve the efficiency of the CZTS solar cells because a Cu-poor composition enhances the formation of Cu vacancies, forming shallow acceptors in the CZTS, while a Zn-rich condition suppresses the substitution of Cu at Zn sites, resulting in relatively deep acceptors [18]. Therefore, CZTS solar cells that are fabricated under Cu-poor and Zn-rich conditions have high conversion efficiencies. The stoichiometric ratios of the best CZTS film herein were Cu/(Zn+Sn)=0.87 and Zn/Sn=1.26, which indicate that the film is highly Cu-poor and Zn-rich, approaching the composition to the best reported CZTS (8.4%) solar cell [19]. The elemental distribution of the films as a function of depth was probed by EDX, and a depth profile of the four elements is shown in Fig. 1(d) for co-sputtering power of 35 W.

Energy-dispersive EDX mappings and line scans were also performed on cross-sections using an acceleration voltage of 10 kV. The EDX depth profile along the film direction reveals homogeneous composition of each element within the CZTS film grown by the one-step fabrication. It can be seen that the copper, zinc, tin, and sulfur concentrations stay constant within the accuracy of the measurement, as indicated by the almost constant relative elemental ratios of the four elements through the CZTS thin film.

Fig. 2 shows the XPS spectra for the four constituent elements of Cu(I), Sn(IV), Zn(II), S (sulfide phase). High-resolution core-level spectra were recorded for the Cu_{2p} region, Zn_{2p} region, Sn_{3d} region, and the S_{2p} region to determine the valence state [20,21]. It can be observed that the binding energies (BE) for Cu $2p_{3/2}$ and Cu $2p_{1/2}$ are 932.5 and 952.3 eV, respectively, with peak splitting of 19.8 eV, as shown in Fig. 2(a). The binding energy peak of the CZTS film was also reported at 932.5 eV, corresponding to the Cu $2p_{3/2}$ core level in CZTS [22,24]. Therefore, it can be considered that only Cu^+ exists in the sample, indicating that the Cu^{2+} of the starting material is reduced during the ionic reaction. Also, the Cu $2p_{3/2}$ and Cu LMM values, as compared with those reported in the literature of [22–24] fall within the region of Cu(I), indicating that copper is in the +1 oxidation state. Shake-up peaks may occur when the outgoing photoelectron simultaneously interacts with a valance electron and excites it to a higher energy level. The kinetic energy of the shake-up core electron is then slightly reduced, giving a satellite structure a few eV below (higher on the calculated BE scale) the core-level position [25]. If the oxidation states of cations and anions is maintained going from CZTS to defected CZTS materials, only a few substitutions can be envisioned to account for the charge balance in non-stoichiometric CZTS, i.e., Cu/(Zn+Sn) < 1 and Zn/Sn > 1 in the study, copper vacancies were expected to be counterbalanced with Zn^{2+} cations in excess. From an electrostatic stability point of view, it was suggested that the substitution process could be $Cu^+(2a)+Cu^+(2c) \rightarrow Zn^{2+}(2c)+V_{Cu}(2a)$ instead of $2Cu^+(2a) \rightarrow Zn^{2+}(2a)+V_{Cu}(2a)$. Thus, substitution processes could be envisioned: (i) two Cu^+ cations are replaced by one Zn^{2+} cation located at the 2a site,
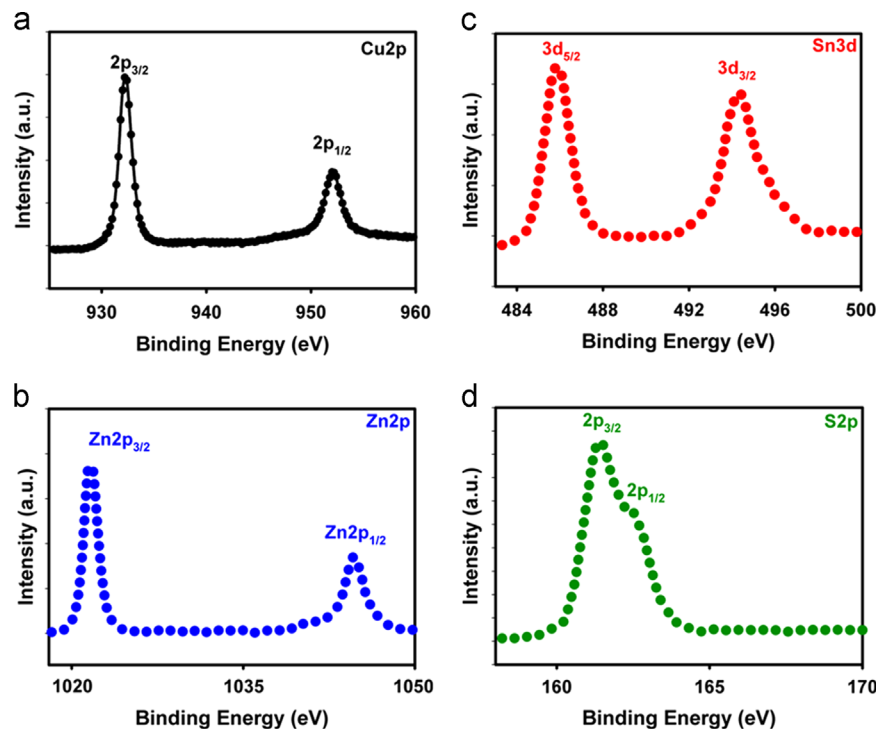

Fig. 2. The XPS spectra of CZTS films (a) core-level spectrum for Cu 2p, (b) core-level spectrum for Zn 2p, (c) core-level spectrum for Sn 3d, and (d) core-level spectrum for S 2p.

leading also to one vacancy on this site [formally $2Cu^+$ (2a) $\leftrightarrow Zn^{2+}$ (2a)$+V_{Cu}$ (2a)]; (ii) one Cu^+ cation is removed from the 2a site, leading to one vacancy on this site, while one $Cu+$ cation is replaced by one Zn^{2+} cation on the 2c site [formally Cu^+ (2a)$+$ Cu^+(2c)$\leftrightarrow Zn^{2+}$(2c)$+V_{Cu}$ (2a)]. Thus, the revision was performed with Cu on the 2a site and Cu/Zn on the 2c site, with the site occupancy factors (sof) being constrained to achieve the charge balance, i.e., $sof(Cu_{2a})+sof(Zn_{2c})=1$ and $sof(Cu_{2c})+sof(Zn_{2c})=1$. The peaks of Zn 2p that appeared at binding energies of 1021.3 eV ($2p_{3/2}$) and 1044.6 eV ($2p_{1/2}$) with a peak splitting of 23.3 eV can be assigned to Zn(II) [21,24]. The Sn $3d_{5/2}$ and $3d_{3/2}$ peaks located at 485.8 and 494.3 eV, respectively, with peak splitting of 8.5 eV, indicate Sn(IV) [see Fig. 2(c)]. It is assumed that the unknown peak near Sn $3d_{3/2}$ at 496.2 eV is attributed to SnO_2 by checking XPS database [26]. In Fig. 2(d) the binding energies for S $2p_{3/2}$ and S $2p_{1/2}$ are 161.6 eV and 162.6 eV respectively, suggesting that sulfur is in the sulfide state [27,28]. The BE values for Cu, Zn, Sn, and S are consistent with those reported previously [29]. These results are

consistent with the reported values in the literature [21,24]. From the XPS analyses, it is found that the atomic ratios of the deposited films are in good agreement with the EDX results. The XPS analysis confirmed the presence of Cu, Zn, Sn, and S in their expected oxidation states.

Fig. 3 shows SEM images of (a) the top CZTS surface, (b) the cross section of a CZTS film deposited at a co-sputtering of 15 W, (c) the top CZTS surface, (d) the cross section of a CZTS film deposited at a co-sputtering of 25 W, (e) the top CZTS surface, and (f) the cross section of a CZTS film deposited at a co-sputtering of 35 W. In all cases, the crust of the CZTS film is well-fused and dense. All the cross section CZTS films show a dense, compact film quality, and almost without voids. Fig. 3(a) and (b) reveals that the surface morphology of the CZTS films that were deposited at 15 W was almost uniform and fine-grained. Our film had larger and more densely packed grains. In Fig. 3(d), the film shows a homogeneous, polycrystalline and extremely dense morphology without any voids, and consists of grains with uniform size of
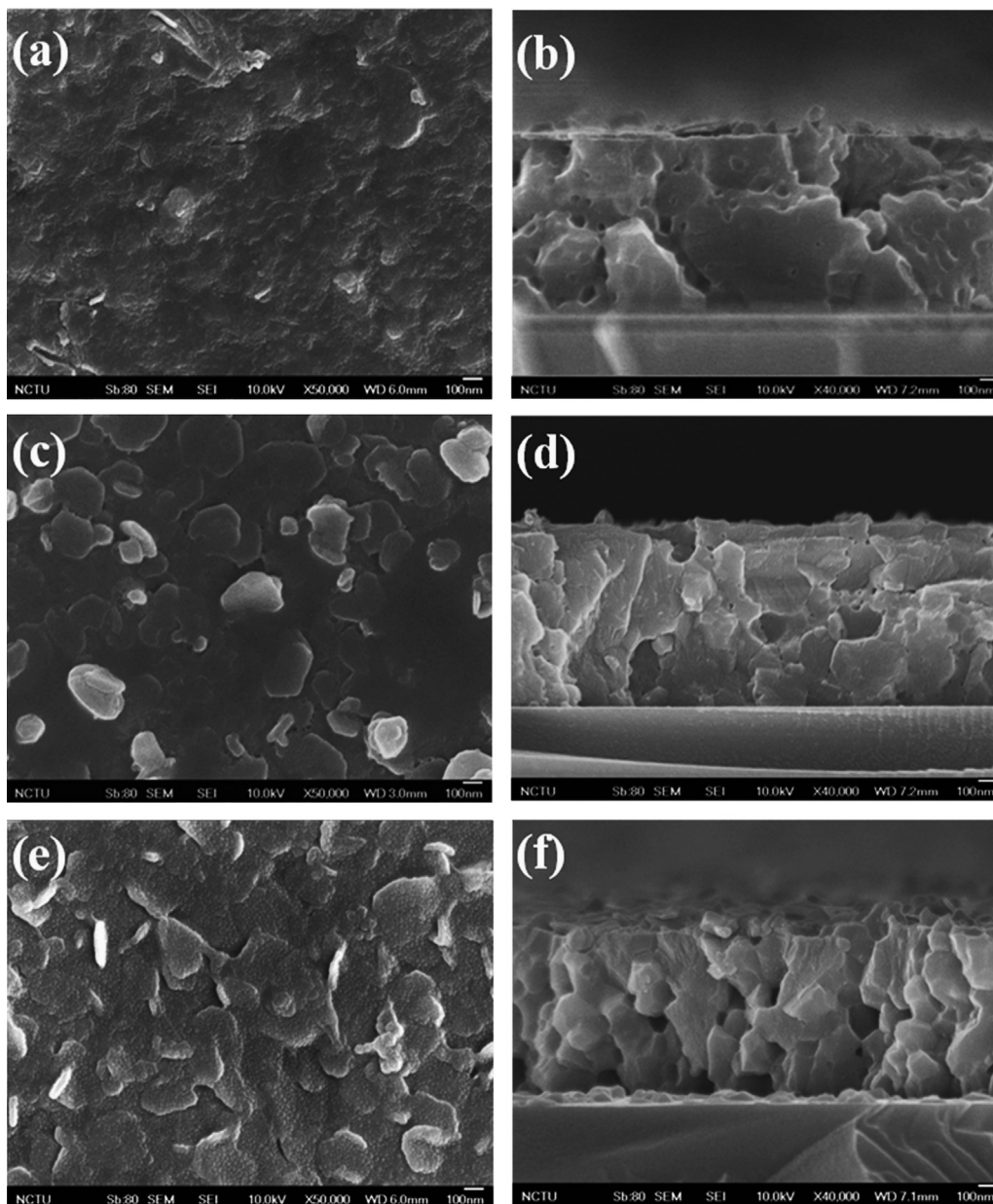

Fig. 3. SEM images of (a) the top CZTS surface, (b) the cross section of a CZTS film deposited a co-sputtering power of 15 W, (c) the top CZTS surface, (d) the cross section of a CZTS film deposited at a co-sputtering power of 25 W, (e) the top CZTS surface, and (f) the cross section of a CZTS film deposited at a co-sputtering power of 35 W.

about 150 nm. As the co-sputtering power was increased to 25 W, a relatively smooth surface and uniformly sized grains in the CZTS thin films were obtained shown in Fig. 3(c) and (d). From the cross-section of the film as shown in Fig. 3(d), it can be seen that film with a thickness of 1500 nm and excellent crystallinity and compactness has been grown on substrate. It should be remarked that columnar grains extending from the bottom to the top of the CZTS layer were observed. This feature is similar to that of CZTS films prepared by thermal evaporation in a vacuum system leading to the highest conversion efficiency of 8.4% [19], and beneficial to decreasing the minority carrier recombination during transport process when applied to solar cell. The Cu and Zn contents of the films could be controlled to produce CZTS films with a homogeneous distribution of sizes of grains large grains and favorable polycrystallinity. For the CZTS films prepared by our co-sputtering condition, the best CZTS film herein were $Cu/(Zn+Sn)=0.87$ and $Zn/Sn=1.26$ which content ratio is the optimal for the best structure. This morphology tendency is consistent with the results of XRD analysis. When the co-sputtering power was increased to 35 W, polygon flakes were observed on the surface of the thin film. In fact, with the highest Zn-excess the entire film is composed of these small grains, as seen in Fig. 3(f). However, EDX reveals that the proportion of the elements Zn/Sn in the thin film then exceed EDX 1.5. According to the literature, such a value may result in an enlarged thin-film band gap of the Zn-rich absorber layer causing the thin film to have similar material characteristics to the those of CuInS, with its wide band gap [30].

Fig. 4a–c presents the XRD patterns of CZTS films with various compositions. The numbers in (a) CZTS-0.97, (b) CZTS-1.26, and (c) CZTS-1.51 indicate the Zn/Sn ratio. CZTS were structurally characterized by XRD with 2θ scanning from 20° to 70°. All three samples yielded sharp crystalline peaks that corresponded to the kesterite or stannite structure. In Fig. 4a–c, the major XRD diffraction peak of (112) is sharp and the small characteristic peaks associated with the kesterite CZTS structure, such as those of (220) and (312) are also clearly observed. The sharp peak at $2\theta=28.48°$ can be attributed to the diffraction by (112) plane of kesterite CZTS and the high intensity of peak revealed strong preferential orientation along (112) plane in the thin film. However, it is difficult to distinguish the structure between kesterite and stannite one due to the fact that the XRD patterns of these two structures differ only slightly in the splitting of high order peaks, such as (220)/(204) and (116)/(312) resulted from the lightly different tetragonal distortion (c/2a) [31]. Only a single phase of kesterite $Cu_2Zn_1Sn_1S_4$ was detected, suggesting that the CZTS films were close to stoichiometry. There were no notable peaks related to secondary phases from XRD, but binary or ternary sulfides such as ZnS, $Cu_{2-x}S$, and $CuSn_xS_y$ have similar diffraction patterns with

CZTS owing to their similar zinc blend-type structures [32]. Fig. 4 inset shows the location and full width at half maximum (FWHM) of (112)-peak XRD patterns for CZTS thin films. The CZTS-1.26 film has a narrower FWHM, which implies that the Zn-rich film with a Zn/Sn ratio of 1.26 has a higher crystalline quality. As the co-sputtering power increased to 25 W, the film microstructure was greatly improved, since the FWHM of the (112) diffraction peak reduced and the peak became much better resolved. The FWHM in the X-ray diffraction pattern is found to decrease with an increase in co-sputtering power indicating that the crystalline nature of the CZTS film improves with increase in co-sputtering power. According to the Scherrer equation, $D=K\lambda/\beta \cos \theta$ (where K, λ, β and θ stand for the constant, the X-ray wavelength, full width at half maximum and diffraction angle, respectively), the average crystallite size (D) of the best CZTS-1.26 sample can be estimated in the range of 60–65 nm. As the co-sputtering power was increased to 35 W, the Zn content also increased. Fig. 4c reveals that the diffraction intensity in the (112) direction is slightly weakened because the excessive amount of Zn reduced the crystallinity of the thin film microstructure, considerably reducing the grain boundaries and weakening crystalline characteristics of the thin film. Typically, semiconductor materials for photovoltaic or transistor applications perform worse in their polycrystalline form because of carrier recombination at the grain boundaries. This is absolutely not true in Cu_2ZnSnS_4 thin film; as a matter of fact it is believed to be opposite, i.e., grain boundaries are beneficial reducing the recombination [33]. Our results reveal that growing CZTS thin films in the absence of binary phase may be advantageous, which may result in large grains and dense films. In addition to the XRD study, a Raman investigation was performed to characterize the samples fully.

Fig. 5 presents the Raman spectra of CZTS absorber films. In the experiment, a strong and sharp quaternary Raman shift at 338 cm^{-1}, characteristic of CZTS, was observed. The Raman spectrum of the annealed sample includes two very small peaks, which are characteristic of the kesterite structure, at 287 cm^{-1} and 368 cm^{-1} [34,35], while the lack of a Raman signal at 476 cm^{-1} reflects the absence of a second-order $Cu_{2-x}S$ phase [36]. In these spectra, no other peak, corresponding to binary copper sulfide SnS_2, ZnS, or Cu_2SnS_3, was observed. This finding suggests that thermal process reduces the number of defects and the number of binary phases. This absence of a second phase can result in homogeneous optoelectronic properties and a low density of recombination centers, further improving the conversion efficiency of solar cells [37,38].

Fig. 6 shows the efficiency distribution map of the CZTS thin film solar cells in the CuS–ZnS–SnS pseudo-ternary phase diagram. The composition ratios of $Cu/(Zn+Sn)$ and Zn/Sn are defined as
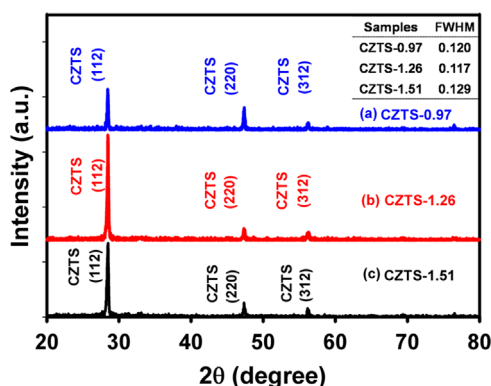

Fig. 4. XRD patterns of annealed CZTS films deposited at co-sputtering powers of (a) 15 W, (b) 25 W, and (c) 35 W.
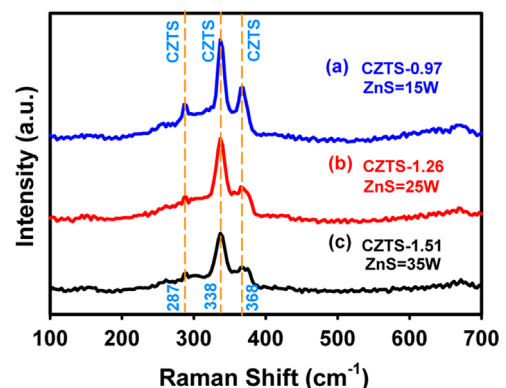

Fig. 5. Raman spectroscopic results of CZTS films deposited at co-sputtering powers of (a) 15 W, (b) 25 W, and (c) 35 W.

the atomic ratio of each constituent element. The colors indicate the efficiency of the solar cells. The efficiency higher than 4% was obtained at the composition ratios Cu/(Zn+Sn) and Zn/Sn appearing in the range of 0.56–1.09 and 1.03–1.76, respectively. Complete devices were formed on samples without adhesion loss and tested under AM1.5 conditions. A conversion efficiency of 5.5% was obtained as the highest in this study. As shown in Fig. 6, the high efficiency samples obtained were significantly nonstoichiometric and had Zn/Sn=1.26 and Cu/(Zn+Sn)=0.87. Literature reports indicate however that the optimal elemental ratios for higher quality CZTS solar cells are in the vicinity of Cu/(Zn+Sn)=0.8 and Zn/Sn=1.2 respectively [39–42], a finding that we find our results consistent with. Although the efficiency reports here on optimal Cu/(Zn+Sn) and Zn/Sn ratios vary in the pseudo-ternary phase

diagram, it appears that Zn-rich and Cu-poor compositions are desired for better performance in CZTS solar cells. The poorer cell performance of CZTS device fabricated at the composition ratios Cu/(Zn+Sn)=0.95 and Zn/Sn=0.97 than of the cell fabricated Cu-poor and Zn-rich compositions was found due to the Zn-poor condition release the substitution of Cu at Zn sites, resulting in relatively deep acceptors. The acceptors are attributed to the intrinsic defects of V_{Cu} and Cu_{Zn}, which have the activation energy of 0.57 and 0.01 eV, respectively. Therefore, Cu_{Zn} will dominate over V_{Cu} in CZTS films. However, this situation may not be optimal for solar cell applications due to the relatively deep acceptor level of Cu_{Zn}. The relatively low efficiency resulted from the inaccurate atomic composition which was maybe caused by the cracks and holes on the surface of the quaternary CZTS target generated during the sputtering process. Optimization of the stable targets used in high efficiency CZTS devices, such as uniform, density, purity and life, are the possible directions for further improving target performance. Although the pseudo-ternary phase efficiency diagram of the one-step fabricated CZTS device are obtained for a quite scattered compositional now, the investigation on the sputtering process by quaternary alloy target and binary alloy target magnetron co-sputtering is just in the beginning and the improvement on this approach can be expected by further tuning.

To evaluate the improvement of the device performance and loss mechanisms that can be achieved by coating with ZnO nanorod arrays, the EQE of the same solar cell was measured before and after it was thus coated, as presented in Fig. 7a. The EQE increases steeply around 350 nm. This increase in associated with the absorption edge of the ZnO window layer. The second steep increase around 500 nm is related to the absorption edge of the CdS buffer layer. A maximum quantum efficiency of 76% is obtained at a photon wavelength of 540 nm; at higher wavelengths, the curve exhibits a long tail from 700 nm, indicating a small electron diffusion length. The estimated optical band gap of the CZTS absorber layer, which is determined by plotting $[E \times \ln(1-EQE)]^2$ vs E and extrapolating the straight line portion of the
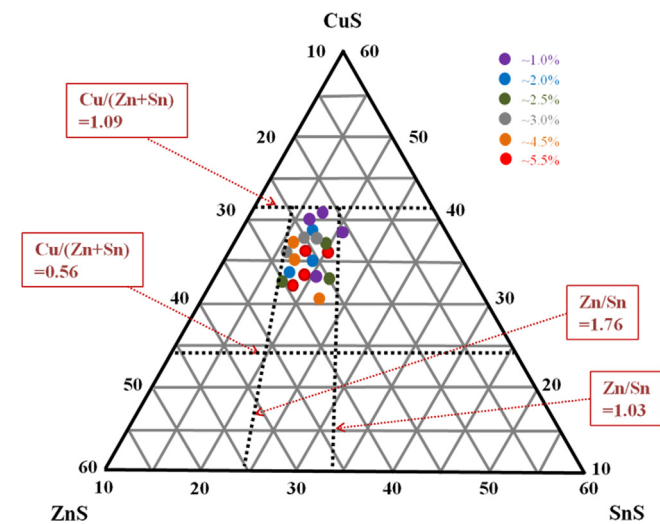

Fig. 6. Efficiency map of CZTS thin film solar cells in the CuS–ZnS–SnS pseudo-ternary phase diagram.
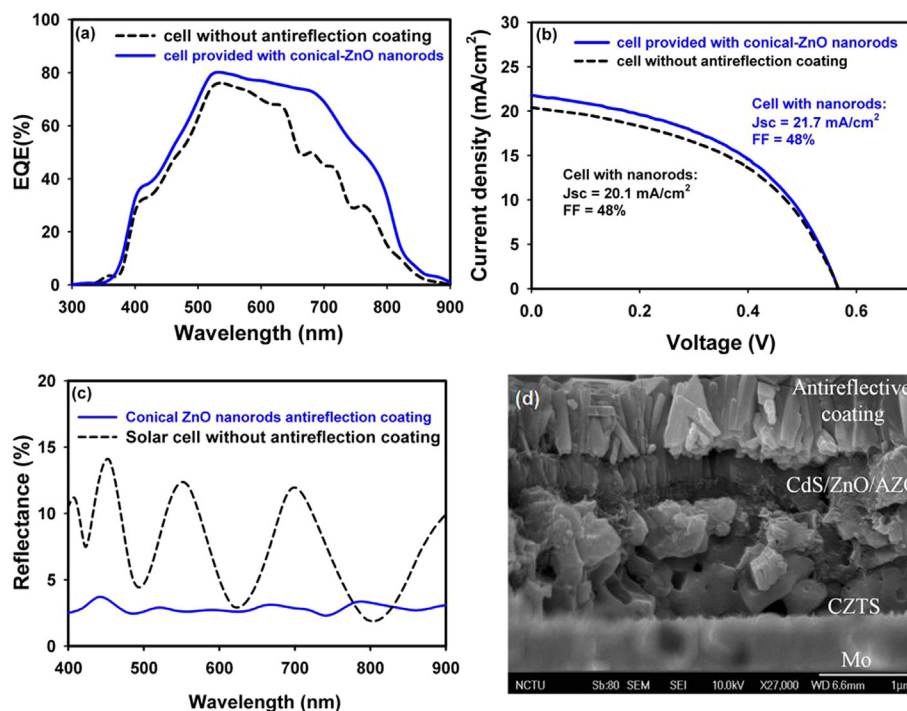

Fig. 7. (a) External quantum efficiency of CZTS solar cell without (black dotted line) and with (blue line) antireflection coating of conical ZnO nanorods. (b) J–V characteristics of CZTS solar cell with and without antireflection coating of conical ZnO nanorods. (c) Wavelength-dependent reflectance of CZTS solar cell before (black dotted line) and after (blue line) deposition of antireflection coating of conical ZnO nanorods. (d) The cross-sectional FESEM image of the fabricated CZTS solar cell. (For interpretation of the references to color in this figure legend, the reader is referred to the web version of this article.)

graph to the *E*-axis, is 1.51 eV, agreeing closely with two recent theoretical calculations [43]. However, coating with conical ZnO nanorods improved the quantum efficiency at wavelengths from 450 nm to 850 nm. The reflectance of conical ZnO nanorod-coated cells is independent of the wavelengths of the incident photons. The bumps in quantum efficiency, which are related to the interference fringes in Fig. 7a, were improved by using of conical ZnO nanorod arrays, which increased the short-circuit current by 8.6% without any significant effect on the open-circuit voltage. Fig. 7b plots the measured current–voltage characteristics. The presence of the conical ZnO nanorod layer improved the short-circuit current by 8.6%. The light conversion efficiency of the solar cells was improved from 5.5% to 6% by using aligned conical ZnO nanorod arrays as an antireflection layer. However, the relatively low photocurrent was due to low quantum efficiency at long wavelength region (Fig. 7a).The decrease in the long wavelength response can be attributed to the increased carrier recombination in the bulk of CZTS layers due to the poor crystalline quality. There are obvious improvement in photocurrent and efficiency enhancement. These are mainly caused by both the reduction of light reflectance and surface recombination centers by window layer [44]. Fig. 7c presents the optical reflectance of the conical-ZnO nanorod-coated solar cell and the bare CZTS solar cell. The results reveal that more photons were absorbed by the nanorod array structure, because of its steep gradual refractive index profile and its excellent light-trapping ability [45,46]. Fig. 7d presents cross-section FE-SEM image of the fabricated CZTS solar cell coated with conical-ZnO nanorods. The length of the conical-ZnO nanorods is approximately 500 nm and their average diameter is approximately 50 nm with a broad size distribution. It was recognized that the size and the shape of nanorods grown on the CZTS thin film solar cell satisfy the theoretical requirements for the efficient antireflection coating fabrication [47–49]:

(1) The height (h) must not be smaller than 40% of the longest operational wavelength (λ): $h \geq 0.4\lambda$. (2) The center-to-center spacing (Λ) of the nanorod structure must be smaller than the shortest operational wavelength (λ) divided by material refractive index (n): $\Lambda < \lambda/n$. The images show that the CZTS absorber layer is dense and polycrystalline. Also, an array of densely distributed ZnO nanorods aggregates on the top of CZTS solar cell, fully covering the AZO window layer.

4. Conclusions

In summary, the deposition of Cu_2ZnSnS_4 films by the co-sputtering of quaternary with binary targets is proposed. Working devices that use such a sputtered film without the need for any additional sulfur source during or after deposition are fabricated. The Cu_2ZnSnS_4 films are dense smooth morphology, polycrystalline kesterite structure, and (112) highly-oriented. The as-obtained CZTS solar cells possess the power conversion efficiency of 5.5% on a Cu-poor and Zn-rich condition and the efficiency has been further improved to 6% by employing the nanorods structure on the top of window layer. This ZnO nanorod coating leads to a decrease of the average reflectance of the solar cells. It boosts the solar cells short-circuit current up to 8.6% without significant effect on their open-circuit voltage and fill factor (FF), although the processing details are not yet optimized. Optimization of other layers and the approaches used in high efficiency Cu_2ZnSnS_4 devices, such as absorbing layer stoichiometry and junction band engineering, are the possible directions for further improving device performance. This research will contribute to the development of multi-element compound targets, the commercialization of Cu_2ZnSnS_4 solar cells, and the development of the nano manufacturing of non-sulfurized Cu_2ZnSnS_4 solar cells. Owing to the rapidity of production by sputtering, the price of solar cells may be greatly reduced, supporting future mass production and providing considerable economic benefits.

References

[1] M.A. Green, K. Emery, Y. Hishikawa, W. Warta, Solar cell efficiency tables (version 37), Prog. Photovolt.: Res. Appl. 19 (2011) 84–92.
[2] H. Katagiri, K. Jimbo, W.S. Maw, K. Oishi, M. Yamazaki, H. Araki, A. Takeuchi, Development of CZTS-based thin film solar cells, Thin Solid Films 517 (2009) 2455–2460.
[3] D.B. Mitzi, O. Gunawan, T.K. Todorov, K. Wang, S. Guha, The path towards a high-performance solution-processed kesterite solar cell, Sol. Energy Mater. Sol. Cells 95 (2011) 1421–1436.
[4] W. Shockley, H.J. Queisser, Detailed balance limit of efficiency of p–n junction solar cells, J. Appl. Phys. 32 (1961) 510–519.
[5] A. Emrani, P. Vasekar, C.R. Westgate, Effects of sulfurization temperature on CZTS thin film solar cell performances, Sol. Energy 98 (2013) 335–340.
[6] T.P. Dhakal, C.–Y. Peng, R.R. Tobias, R. Dasharathy, C.R. Westgate, Characterization of a CZTS thin film solar cell grown by the sputtering method, Sol. Energy 100 (2014) 23–30.
[7] W.-C. Hsu, I. Repins, C. Beall, C. DeHart, B. To, W. Yang, Y. Yang, R. Noufi, Growth mechanisms of co-evaporated kesterite: a comparison of Cu-rich and Zn-rich composition paths, Prog. Photovol.: Res. Appl. 22 (2014) 35–43.
[8] M. Guc, R. Caballero, K.G. Lisunov, N. López, E. Arushanov, J.M. Merino, M. León, Disorder and variable-range hopping conductivity in Cu_2ZnSnS_4 thin films prepared by flash evaporation and post-thermal treatment, J. Alloys Compd. 596 (2014) 140–144.
[9] J. Ge, J. Jiang, P. Yanga, C. Penga, Z. Huang, S. Zuo, L. Yang, J. Chu, A 5.5% efficient co-electrodeposited $ZnO/CdS/Cu_2ZnSnS_4/Mo$ thin film solar cell, Sol. Energy Mater. Sol. Cells 125 (2014) 20–26.
[10] S.G. Lee, J. Kim, H.S. Woo, Y. Jo, A.I. Inamdar, S.M. Pawar, H.S. Kim, W. Jung, H.S. Im, Structural, morphological, compositional, and optical properties of single step electrodeposited Cu_2ZnSnS_4 (CZTS) thin films for solar cell application, Curr. Appl. Phys. 14 (2014) 254–258.
[11] Z. Su, K. Sun, Z. Han, H. Cui, F. Liu, Y. Lai, J. Li, X. Hao, Y. Liu, M.A. Green, Fabrication of Cu_2ZnSnS_4 solar cells with 5.1% efficiency via thermal decomposition and reaction using a non-toxic sol–gel route, J. Mater. Chem. A 2 (2014) 500–509.
[12] S. Kahraman, S. Çetinkaya, H.A. Çetinkara, H.S. Güder, A comparative study of Cu_2ZnSnS_4 thin films growth by successive ionic layer adsorption–reaction and sol–gel methods, Thin Solid Films 550 (2014) 36–39.
[13] T.K. Todorov, K.B. Reuter, D.B. Mitzi, High-efficiency solar cell with earth-abundant liquid-processed absorber, Adv. Energy Mater. 22 (2010) E156–E159.
[14] M. Yao, C.W. Shi, Y.R. Zhang, X.Y. Dai, Deposition of Cu_2ZnSnS_4 thin film by pulsed laser deposition and assembly of thin film solar cell with the novel structure of $FTO/CdS/Cu_2ZnSnS_4/Mo$, Adv. Mater. Res. 716 (2013) 328–331.
[15] G.D. Surgina, A.V. Zenkevich, I.P. Sipaylo, V.N. Nevolin, W. Drube, P.E. Teterin, M.N. Minnekaev, Reactive pulsed laser deposition of Cu_2ZnSnS_4 thin films in H_2S, Thin Solid Films 535 (2013) 44–47.
[16] T.K. Todorov, J. Tang, S. Bag, O. Gunawan, T. Gokmen, Y. Zhu, D.B. Mitzi, Beyond 11% efficiency: characteristics of state-of-the-art $Cu_2ZnSn(S,Se)_4$ solar cells, Adv. Energy Mater. 3 (2013) 34–38.
[17] I. Repins, C. Beall, N. Vora, C. DeHart, D. Kuciauskas, P. Dippo, B. To, J. Mann, W.-C. Hsu, A. Goodrich, R. Noufi, Co-evaporated $Cu_2ZnSnSe_4$ films and devices, Sol. Energy Mater. Sol. Cells 101 (2012) 154–159.
[18] S. Chen, X.G. Gong, A. Walsh, S. Wei, Defect physics of the kesterite thin-film solar cell absorber Cu_2ZnSnS_4, Appl. Phys. Lett. 96 (2010) 021902–021904.
[19] B. Shin, O. Gunawan, Y. Zhu, N.A. Bojarczuk, S.J. Chey, S. Guha, Thin film solar cell with 8.4% power conversion efficiency using an earth-abundant Cu_2ZnSnS_4 absorber, Prog. Photovolt.: Res. Appl. 21 (2013) 72–76.
[20] S.C. Riha, B.A. Parkinson, A.L. Prieto, Solution-based synthesis and characterization of Cu_2ZnSnS_4 nanocrystals, J. Am. Chem. Soc. 131 (2009) 12054–12055.
[21] A. Singh, H. Geaney, F. Laffir, K.M. Ryan, Colloidal synthesis of wurtzite Cu_2ZnSnS_4 nanorods and their perpendicular assembly, J. Am. Chem. Soc. 134 (2012) 2910–2913.
[22] C. Chory, F. Zutz, F. Witt, H. Borchert, J. Parisi, Synthesis and characterization of Cu_2ZnSnS_4, Phys. Status Solidi (c) 7 (2010) 1486–1488.
[23] T. Ghodselahi, M.A. Vesaghi, A. Shafiekhani, A. Baghizadeh, M. Lameii, XPS study of the $Cu@Cu_2O$ core–shell, Nanoparticles 255 (2008) 2730–2734.
[24] H. Jiang, P. Dai, Z. Feng, W. Fana, J. Zhan, Phase selective synthesis of metastable orthorhombic Cu_2ZnSnS_4, J. Mater. Chem. 22 (2012) 7502–7506.
[25] S. Li, H. Wang, W. Xu, H. Si, X. Tao, S. Lou, Z. Du, L.S. Li, Synthesis and assembly of monodisperse spherical Cu_2S nanocrystals, J. Colloid Interface Sci. 330 (2009) 483–487.

[26] NIST X-ray Photoelectron Spectroscopy Database, http://srdata.nist.gov/xps/Default.aspx.

[27] S.C. Riha, B.A. Parkinson, A.L. Prieto, Solution based synthesis and characterization of Cu_2ZnSnS_4 nanocrystals, J. Am. Chem. Soc. 131 (2009) 12054–12055.

[28] P. Dai, X. Shen, Z. Lin, Z. Feng, H. Xua, J. Zhan, Band-gap tunable $(Cu_2Sn)_{x/3}$ $Zn_{1-x}S$ nanoparticles for solar cells, Chem. Commun. 46 (2010) 5749–5751.

[29] X. Zhang, X. Shi, W. Ye, C. Ma, C. Wang, Electrochemical deposition of quaternary Cu_2ZnSnS_4 thin films as potential solar cell material, Appl. Phys. A 94 (2009) 381–386.

[30] S. Schorr, V. Riede, D. Spemann, Th. Doering, Electronic band gap of $Zn_{2x}(CuIn)_{1-x}X_2$ solid solution series (X=S, Se, Te), J. Alloys Compd. 414 (2006) 26–30.

[31] Q. Guo, H.W. Hillhouse, R. Agrawal, Synthesis of Cu_2ZnSnS_4 nanocrystal ink and its use for solar cells, J. Am. Chem. Soc. 131 (2009) 11672–11673.

[32] A. Wangperawong, J.S. King, S.M. Herron, B.P. Tran, K. Pangan-Okimoto, S.F. Bent, Aqueous bath process for deposition of Cu_2ZnSnS_4 photovoltaic absorbers, Thin Solid Films 519 (2011) 2488–2492.

[33] J.B. Li, V. Chawla, B.M. Clemens, Investigating the role of grain boundaries in CZTS and CZTSSe thin film solar cells with scanning probe microscopy, Adv. Mater. 24 (2012) 720–723.

[34] H. Yoo, J. Kim, Comparative study of Cu_2ZnSnS_4 film growth, Sol. Energy Mater. Sol. Cells 95 (2011) 239–244.

[35] P.A. Fernandes, P.M.P. Salome, A.F. da Cunh, Growth and Raman scattering characterization of Cu_2ZnSnS_4 thin films, Thin Solid Films 517 (2009) 2519–2523.

[36] P.M.P. Salomé, J. Malaquias, P.A. Fernandes, M.S. Ferreira, A.F. da Cunha, J.P. Leitão, J.C. González, F.M. Matinaga, Growth and characterization of $Cu_2ZnSn(S,Se)_4$ thin films for solar cells, Sol. Energy Mater. Sol. Cells 101 (2012) 147–153.

[37] T. Tanaka, T. Nagatomo, D. Kawasaki, M. Nishio, Q. Guo, A. Wakahara, A. Yoshida, H. Ogawa, Preparation of Cu_2ZnSnS_4 thin films by hybrid sputtering, J. Phys. Chem. Solids 66 (2005) 1978–1981.

[38] A. Nagoya, R. Asahi, Defect formation and phase stability of Cu_2ZnSnS_4 photovoltaic material, Phys. Rev. B 81 (2010) 113202–113205.

[39] T.K. Todorov, K.B. Reuter, D.B. Mitzi, High-efficiency solar cell with earth-abundant liquid-processed absorber, Adv. Mater. 22 (2010) E156–E159.

[40] A. Ennaoui, M. Lux-Steiner, A. Weber, D. Abou-Ras, I. Ko tschau, H.-W. Schock, R. Schurr, A. Holzing, S. Jost, R. Hock, T. Voß, J. Schulze, A. Kirbs, Cu_2ZnSnS_4 thin film solar cells from electroplated precursors: novel low-cost perspective, Thin Solid Films 517 (2009) 2511–2514.

[41] K. Tanaka, M. Oonuki, N. Moritake, H. Uchiki, Thin film solar cells prepared by non-vacuum processing, Sol. Energy Mater. Sol. Cells 93 (2009) 583–587.

[42] Q. Guo, G.M. Ford, W. Yang, B.C. Walker, E.A. Stach, H.W. Hillhouse, R. Agrawal, Fabrication of 7.2% efficient CZTSSe solar cells using CZTS nanocrystals, J. Am. Chem. Soc. 132 (2010) 17384–17386.

[43] S. Chen, X.G. Gong, A. Walsh, S.H. Wei, Crystal and electronic band structure of Cu_2ZnSnX_4 (X=S and Se) photovoltaic absorbers: First-principles insights, Appl. Phys. Lett. 94 (2009) 041903–041905.

[44] S.H. Baek, H.S. Jang, J.H. Kim, Characterization of optical absorption and photovoltaic properties of silicon wire solar cells with different aspect ratio, Curr. Appl. Phys. 11 (2011) S30–S33.

[45] Y.C. Chao, C.Y. Chen, C.A. Lin, J.H. He, Light scattering by nanostructured anti-reflection coatings, Energy Environ. Sci. 4 (2011) 3436–3441.

[46] B. -K. Shin, T. -I. Lee, J. Xiong, C. Hwang, G. Noh, J.-H. Cho, J.-M. Myoung, Bottom-up grown ZnO nanorods for an antireflective moth-eye structure on $CuInGaSe_2$ solar cells, Sol. Energy Mater. Sol. Cells 95 (2011) 2650–2654.

[47] M.Y. Hsieh, S.Y. Kuo, H.V. Han, J.F. Yang, Y.K. Liao, F.I. Lai, H.C. Kuo, Enhanced broadband and omnidirectional performance of $Cu(In,Ga)Se_2$ solar cells with ZnO functional nanotree arrays, Nanoscale 5 (2013) 3841–3846.

[48] D. Raguin, G. Morris, Antireflection structured surfaces for the infrared spectral region, Appl. Opt. 32 (1993) 1154–1167.

[49] B. Thornton, Limit of the moth's eye principle and other impedance-matching corrugations for solar-absorber design, J. Opt. Soc. Am. 65 (1975) 267–270.